JOURNAL OF SPACECRAFT AND ROCKETS
Vol. 31, No. 3, May–June 1994

Multiblock Analysis for Shuttle Orbiter Re-entry Heating from Mach 24 to Mach 12

Peter A. Gnoffo* and K. James Weilmuenster*
NASA Langley Research Center, Hampton, Virginia 23681
and
Stephen J. Alter†
Lockheed Engineering & Sciences Company, Hampton, Virginia 23665

A multiblock, laminar heating analysis for the Shuttle Orbiter at three trajectory points ranging from Mach 24.3 to Mach 12.86 on re-entry is described. The analysis is performed using the Langley Aerothermodynamic Upwind Relaxation Algorithm with a seven species chemical nonequilibrium model. A finite-catalytic-wall model appropriate for shuttle tiles at a radiative equilibrium wall temperature is applied. Computed heating levels are generally in good agreement with the flight data, although a few rather large discrepancies remain unexplained. The multiblock relaxation strategy partitions the flowfield into manageable blocks requiring a fraction of the computational resources (time and memory) required by a full domain approach. In fact, the computational cost for a solution at even a single trajectory point would be prohibitively expensive at the given resolution without the multiblock approach. Converged blocks are reassembled to enable a fully coupled converged solution over the entire vehicle, starting from a nearly converged initial condition.

Nomenclature

C_A = axial force coeficient
C_m = pitching-moment coeficient
C_N = normal force coeficient
h = altitude, km
i, j, k = computational cell indices
M_∞ = freestream Mach number
n = iteration level index
p = pressure, nondimensionalized by $\rho_\infty V_\infty^2$
q = convective heating, W/m^2
T = temperature, K
V_∞ = freestream velocity, m/s
x, y, z = Cartesian coordinates, in.
α = angle of attack, deg
δ_{bf} = bodyflap deflection, deg
δ_{el} = elevon deflection, deg
ϵ = surface emissivity
η = relaxation parameter for radiative equilibrium wall boundary condition
ρ_∞ = freestream density, kg/m^3
σ = Stefan-Boltzmann constant, W/(m^2 − K^4)

Introduction

THE space transportation system (STS) was designed in an era in which large scale, computational fluid dynamic (CFD) analyses were unavailable to assist in the design process. The 1970s CFD capabilities were crude by today's standards, but they played a critical role in flying STS-1. The analyses were predominantly used to verify that the design methodology was conservative, and they were generally restricted to the windward surface, forward of the bow/wing shock–shock interaction region. A review of some of these analyses can be found in Refs. (1–3).

Supercomputer technology has now progressed to the point where CFD has the resources (speed and memory) to make substantial contributions to future hypersonic vehicle design projects by providing flowfield solutions over complete, winged configurations. These solutions provide surface pressure and heating predictions at selected design points, but, more importantly, they also provide insight into the very flow structure with powerful, graphical analysis tools that show streamline traces, vorticity distributions, profile information, and the like. CFD analyses are being used now, for example, in the National AeroSpace Plane (NASP) project. They are expected to play an important role in the design of future elements of our space transportation system.

The capabilities and limitations of CFD simulations for hypersonic flow over winged vehicles must be periodically re-evaluated to account for advances in algorithms and computational power and to include updates to the database for code validation. The importance of such activity is internationally recognized.[4,5] The database obtained by the Orbiter experiments (OEX) program on board the Orbiters Columbia and Challenger provides a crucial benchmark for such evaluations. The objective of this paper (and companion papers[6–8]) is to perform this evaluation for the Langley Aerothermodynamic Upwind Relaxation Algorithm (LAURA)[9,10] using the OEX benchmark. The database emphasized herein is heat transfer from the STS-2 flight.[11] Some calculations for the STS-1 flight were also made for the purpose of investigating the pitching-moment anomaly, discussed in more detail in the companion paper,[8] along with aerodynamic coefficient data.

Details of the study follow in later sections but the general approach taken is to define three trajectory point CFD benchmarks that can efficiently utilize the computer power (processors, in-core memory, fast solid-state-device [SSD] memory) available at the inception of this study (8 processors, 128MW) in the multiuser environment on the NASA Langley Cray Y-MP and the NAS Cray Y-MP. A multiblock analysis allows different pieces of the whole to be computed separately (and in most cases, concurrently). The chemical nonequilibrium anal-

Received Aug. 24, 1993; revision received Jan. 20, 1994; accepted for publication Jan. 27, 1994.

*Aerospace Engineer, Aerothermodynamics Branch, Space Systems Division. Associate Fellow AIAA.
†Aeronautical Engineer. Member AIAA.

yses include seven species (N, O, N_2, O_2, NO, NO^+, and e^-). Finite-rate wall catalysis appropriate for shuttle tiles and a radiative equilibrium wall temperature are applied. One thermal nonequilibrium case is computed that employs a two-temperature model. Another equilibrium case is computed that employs thermodynamic and transport property curve fits.

Computational Grid

A surface grid defined by 150 cells from the nose to the wing-fuselage-tail trailing edge and by 109 circumferential cells is employed. This grid includes the correct elevon deflections for each trajectory point, as well as the orbital maneuvering system (OMS) pods and the vertical tail. The bodyflap is defined by an additional 30 × 14 cells. The shock layer is resolved with 60 cells. Spatial grid convergence studies for a closely related test case were reported.[6] Grid requirements defined by that study have been employed in the present work. A grid convergence study confined to the first 500 inches of the vehicle because of memory limitations is described in a later section.

Details of the baseline grid generation process are presented in Ref. 8. After the grid is generated, LAURA has the capability to redistribute mesh points across the shock layer and to align the outer boundary with the captured shock as the solution evolves.[12] The cell Reynolds number[9,12] at the wall is set to 3.0. The redistribution is particularly important because the volume grid generator was severely restricted in its ability to generate grids with adequate resolution near the wall. However, the one-dimensional adaption was unable to improve the grid in the vicinity of the vertical tail, including most of the OMS pods. Because the grid is insufficiently clustered in these areas, heating predictions are not presented over these elements.

Multiblock Analysis

The multiblock solution strategy is applied in two stages. The first stage may be regarded as a space-marching solution, like the parabolized-Navier-Stokes (PNS) methods, except that three-dimensional data blocks are employed rather than two-dimensional data planes. The second stage is a conventional, global relaxation that uses the first stage solution as an initial condition. The advantages of the three-dimensional block marching over two-dimensional block marching are that: 1) solution robustness is not sacrificed when employing second-order discretization in the streamwise direction; and 2) embedded subsonic pockets and shock/boundary-layer interactions are easily computed, provided that the outflow boundary of the subdomain is intelligently chosen (i.e., supersonic outflow). Embedded subsonic pockets can be computed because pseudo-temporal, point-implicit relaxation is used to obtain the steady solution. The subdomain boundaries are easily tailored to the physics of a given application. The advantage of the two-dimensional block marching is that if the flow is sufficiently well behaved (i.e., supersonic streamwise flow above the boundary layer and insignificant perturbations moving upstream through the boundary layer), then the stage one computation can be an order of magnitude faster than conventional, global relaxation. The tradeoffs between marching strategies are not explored in this work.

The nose region is solved for the first stage on a (15 × 109 × 60) cell grid using extrapolation outflow boundary conditions. This domain fully contains the sonic line, except for a very narrow subsonic region in the boundary layer. Grid adaption routines are used to align the volume grid with the captured bow shock. The next windside block extends 50 cells from $i = 14$ (two planes inside the nose domain) to $i = 63$ (ahead of the wing) and from $j = 70$ (circumferential plane approximately behind the wing leading edge and fuselage corner) to $j = 109$ (the windside symmetry plane). Subsequent windside blocks extend from $i = 62$ to $i = 111$ (just past the wing tip leading edge) and from $i = 110$ to $i = 150$ (the wing/elevon trailing edge). The block boundaries on the surface for stage 1 are shown in Fig. 1.

The exit plane solution from the previously converged upwind block is used to initialize the next windside block. The exit plane solution is simply injected, plane by plane, into this new block. Furthermore, the k-directional grid distribution in the new block is reset to match that of the upwind block, which has already experienced several applications of the grid adaption routine. This injection speeds the development of a converged boundary-layer profile as compared to conventional, unstaged, global relaxation techniques. Only a single plane of data is required from the upstream block to serve as an inflow boundary condition. Extrapolation is again used for the outflow boundary. The side boundary condition at $j = 70$ depends on the value of the component of Mach number normal to this plane. If this component is supersonic, the usual case for the given orientation of the side plane and the high angle of attack, then simple extrapolation provides a well-posed boundary condition. If this component is subsonic, then a temporary fix is applied that forces a supersonic expansion (see Boundary Conditions).

Leeside blocks are marched in the same manner as the windside blocks, except that the side plane extrapolation boundary condition is replaced with an inflow boundary condition extracted from the interior of a previously converged windside domain (Fig. 1). In the STS-1 cases, the leeside domains have the same range in the streamwise direction as the windside domains, although this correspondence is not generally required. The circumferential range extends from $j = 1$ to $j = 71$. Because the nth leeside block and the $n + 1$th windside blocks are independent, they can be run simultaneously on the computer.

The relatively small memory requirements of these subdomains in stage one generally expedite turnaround on multiuser supercomputers and increase relaxation cycles per CPU hour. Each subdomain was processed using 4–8 CPU hours per run on a Cray Y-MP. Furthermore, the subdomain is divided into eight smaller partitions (one partition per processor using an asynchronous, macrotasked relaxation strategy[10,13]) so that elapsed time is only slightly greater than 0.5 hours for a 4-CPU-hour run. Two to four runs are used to converge each subdomain; the number depending on subjective judgments of satisfactory grid adaption and objective judgment of surface heat-transfer convergence. Surface heat-transfer convergence is judged based on error norms of order 10^{-6} in the boundary layer partitions and predominant overplotting of centerline heating distributions on sequential runs.

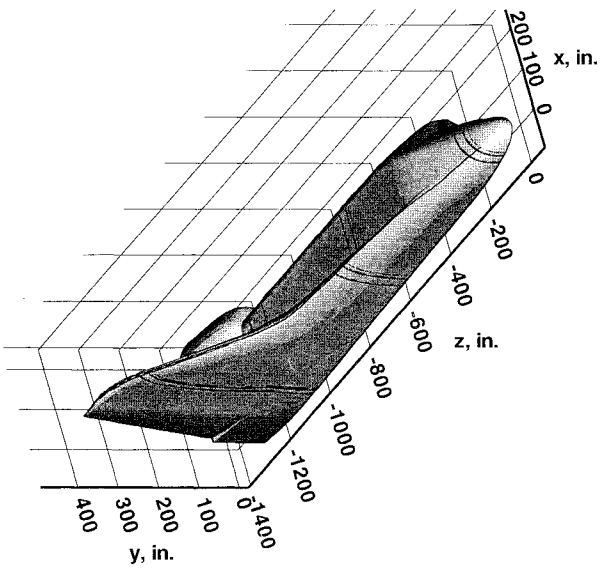

Fig. 1 Block boundaries on surface for stage one computations and associated Cartesian coordinate reference frame.

After each subdomain is converged, the solution is saved in a master copy of the complete domain. The stage two, global relaxation process begins when all the subdomains are filled. In this case, five streamwise zones (average length equal to 30 cells with the last zone involving a special sidewall boundary condition for the vertical tail) are defined (Fig. 2). This partitioning represents the best compromise between task common memory overhead and requirements for an easily vectorized tail boundary condition. On an eight-processor machine, the work of converging the five zones may be divided among eight processors. Because of the greater memory required for the global relaxation, it is necessary to save solution Jacobians on fast, solid-state-device (SSD) memory. The global solution in stage two utilized 128 megawords (MW) of in-core memory, 128 MW of SSD memory, and eight processors working in a fully coupled, macrotasked mode, utilizing on average more than seven concurrent CPUs per hour of elapsed time on a Cray Y-MP. Total CPU time for each case is approximately 150–200 hours on a Cray Y-MP. Elapsed time on the Y-MP is estimated at 80 hours per case because of the extensive use of macrotasking. It is estimated that this two-stage process is approximately a factor of 10 times faster then proceeding from scratch with global relaxation, based on extrapolation of error norm reduction rates of the global solution in earlier test cases.

The solution of the flowfield over the bodyflap must include enough of the body domain to allow for potential upstream interaction caused by the deflected bodyflap. Parts of the windside domain are extracted from the stage 2 solution over the body in order to serve as an inflow boundary for the bodyflap and allow enough area for this interaction. The block boundaries used to compute the flowfield over the deflected bodyflap are shown in Fig. 3.

Two inflow blocks and one sideflow block of one cell in width provide boundary conditions for the bodyflap well away from the interaction zone of the deflected flap. The exit plane and side plane on the actual flap have predominantly supersonic Mach number components normal to the exit surfaces; consequently, extrapolation outflow boundaries are adequate to close the problem. (Preliminary tests for a perfect gas flow windtunnel case that include the near wake about the bodyflap indicate the extrapolation boundary condition results compare well to the full wake results. Tests at flight conditions are pending.)

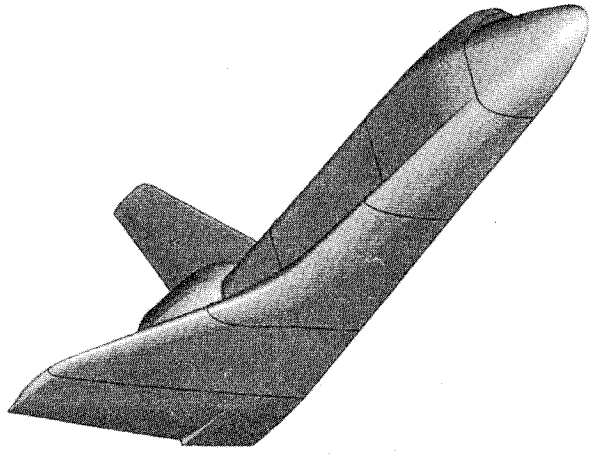

Fig. 2 Block boundaries on surface for stage two computations.

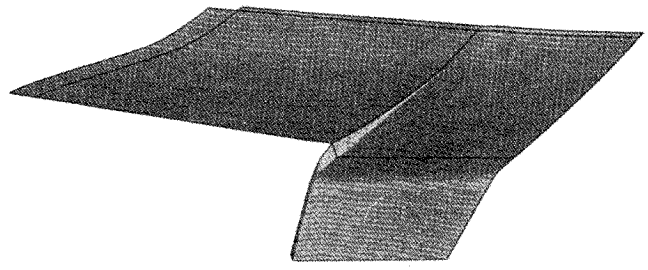

Fig. 3 Block boundaries on surface for the bodyflap computation.

Boundary Conditions

Freestream conditions are given in Table 1 for each of the three selected trajectory points for STS-2. (An STS-1 trajectory point used in the companion study[8] and that served to initialize the STS-2 calculations is also presented. STS-1 results are not presented here because of space limitations and the lack of heating data in flight.) Control surface parameters for the three STS-2 trajectory points are presented in Table 2.

No-slip conditions for velocity and temperature are applied at the wall. The normal pressure gradient at the wall is set to zero. A radiative equilibrium wall boundary condition on temperature is applied as follows in a time-lagged manner for every point on the surface.

$$T_{\text{wall}}^{n+1} = \eta\left[\frac{q^n}{\epsilon\sigma}\right]^{1/4} + (1-\eta)T_{\text{wall}}^{n} \tag{1}$$

where superscripts n and $n+1$ are the global iteration levels. The surface emissivity is set equal to 0.9 for all cases. Variations about this value for the various shuttle surfaces are generally less than 10%. The associated variation of wall temperature with emissivity is less than 3%, assuming that q is only weakly affected by small changes in surface temperature. (Convective heating will be only weakly affected by perturbations in wall temperature when such perturbations are small compared to the difference between the adiabatic wall temperature and the actual wall temperature.) The relaxation factor η is set to 0.01.

Finite-catalytic wall-boundary conditions for chemical nonequilibrium flow, as defined by Zoby et al.[14] for oxygen recombination and by Scott[15] for nitrogen recombination are used for the entire Shuttle surface. (The catalytic qualities of the leeside surface materials have not been characterized; consequently, it was decided to treat the catalytic nature of all surfaces identically to the windside surface.) Similar relations as defined by Stewart et al.[16] for oxygen and nitrogen recombination are tested in selected cases.

All of the above relations for wall catalysis are derived from experimental data established over a limited temperature range. In all cases, temperatures encountered on the leeside are less than the temperatures used to establish the catalytic relations. In the case of Ref. 16, the temperatures on the windside, which average around 1100 K, are less than the lower limit of temperatures (~ 1400 K) used to develop those relations. The analytic models for wall catalysis are evaluated at the local wall temperature in all cases, even when that temperature is outside the experimental base of the model.

Computation of the windside blocks in Stage 1 requires a supersonic outflow into the leeside domain relative to the outflow surface normal vector. Satisfaction of this requirement is

Table 1 Trajectory points

Flight	V_∞ m/s	ρ_∞, kg/m^3	T_∞, K	h, km	M_∞
STS-1	6809	$5.294\ 10^{-5}$	205.8	73.1	23.68
STS-2	6920	$5.750\ 10^{-5}$	202.0	72.4	24.30
STS-2	5617	$1.626\ 10^{-4}$	240.6	64.4	18.07
STS-2	4168	$5.330\ 10^{-4}$	261.6	54.8	12.86

Table 2 Control surface parameters

Flight	M_∞	α, deg	δ_{bf}, deg	δ_{el}, deg
STS-2	24.30	39.4	14.91	1.74
STS-2	18.07	41.2	13.54	1.51
STS-2	12.86	39.7	12.92	0.74

strongly dependent on the grid topology. This requirement was not met in the second windside block in the vicinity of the wing–body junction and caused the solution to diverge. A simple, ad hoc fix to this problem, which preserves the current grid structure and domain boundaries, is to force a supersonic outflow by resetting the pressure in the pseudocell side boundary to 1% of the actual side plane pressure (i.e., $p_{i,69,k} = 0.01p_{i,70,k}$ where the side boundary plane is defined by the $j = 70$ surface). There is no significance to the factor .01, other than that it is small enough to force a supersonic outflow. This fix was only required in the solution of the second windside block. It is not required at all in the second stage of the relaxation process. Some corruption of the solution is expected with this fix; however, in the present case the converged solution in the first stage is not significantly different from the globally relaxed solution with physically correct boundary conditions in the second stage.

Gas Properties

Nonequilibrium Flow—Chemical Model

The chemical nonequilibrium analyses include seven species (N, O, N_2, O_2, NO, NO^+, and e^-). The thermodynamic and transport properties for each of the seven species are obtained from curve fits, as discussed in Ref. 9. The mixing rules for transport properties, including a molar weighted binary diffusion coefficient for each of the species that results in a variable Lewis number is also discussed in Ref. 9. Convective heating to the surface consists of a conductive component proportional to the temperature gradient and diffusive components for each species proportional to the associated mole-fraction gradient as defined within terms 3 and 4 of Eq. 5 in Ref. 9.

The baseline gas kinetic model (used in all test cases) is that of Park as detailed in Table 8.3 of Ref. 17. (Reaction 19 of that table is replaced with the recommended expression given on page 273 of Ref. 17.) A quick check on the effects of a different gas kinetic model based on forward rates recommended by Dunn and Kang[18] and equilibrium constants of Gupta et al.[19] for a Mach 24.3 trajectory point showed minimal effects on surface quantities. Line plots of pressure and heating in the nose region are identical for the two models. Farther downstream, the same line plots would occasionally show differences of less than a few percent.

Nonequilibrium Flow—Thermal Model

The baseline model assumes thermal equilibrium; however, one thermal nonequilibrium case for STS-1 was computed that employed a two-temperature model[9] over the entire vehicle. The effects of thermal nonequilibrium as compared to thermal equilibrium on surface heating and pressure were only evident on the wing, and generally were less than a few percent. The shock-layer thickness over the wing leading edge is only on the order of a few inches, which allows thermal nonequilibrium effects to affect the compression to the wing leading edge and expansion to the windward surface. The related effect to normal and axial drag coefficient is less than 0.6%, but the effect on the moment coefficient is a $\Delta C_m = .00353$ (nose up), roughly corresponding to a change in bodyflap deflection of 0.7 deg based on pitch curves in Ref. 8. More comprehensive tests are required to verify these effects as a general trend.

Equilibrium Flow

A Mach 12.86 trajectory point was computed using the equilibrium air curvefits of Refs. 20 and 21 for thermodynamic and transport properties. The conductive and diffusive components of convective heating for equilibrium flow are combined in a single term involving the enthalpy gradient and reactive Prandtl number as defined by Eq. 5 in Ref. 22. At this Mach number, the effects of the equilibrium model as compared to the nonequilibrium model on aerodynamic coefficients are less than 0.03% for C_N, less than 1.5% for C_A, and $\Delta C_m = .00011$.

Results and Discussion

Baseline Results

Baseline settings for numerical parameters and options in LAURA are: eigenvalue limiter $\epsilon_0 = 0.30$ with aspect ratio scaling across the boundary layer, upwind limiter function as defined in Ref. 6, cell Reynolds number equal to 3 at the wall, and moderate clustering of grid at the captured shock. The baseline settings for physical model options in LAURA have already been discussed in earlier sections; specifically, Park's reaction rates, thermal equilibrium, with catalytic rates from Refs. 14 and 15. Laminar flow is specified.

The STS-2 trajectory points were chosen to span a flight regime in which high-temperature gas chemistry (equilibrium and nonequilibrium) significantly influence aerodynamic and aerothermal loads on the vehicle and because surface heating data are available. Furthermore, the windside flowfield up to the bodyflap is laminar for these trajectory points, as deduced from thermocouple data for this flight. Transition from laminar to turbulent flow does occur on the deflected bodyflap at Mach 18.07 and on the deflected elevons at Mach 12.86. A comprehensive series of comparisons of calculated surface heating with the flight data[11] are presented along longitudinal and transverse surface traces on the shuttle surface. Figures 4–11 present the Mach 24.3 trajectory point comparisons; Figs. 12–21 present the Mach 18.07 trajectory point comparisons; and Figs. 22–29 present the Mach 12.86 trajectory point comparisons. The fig-

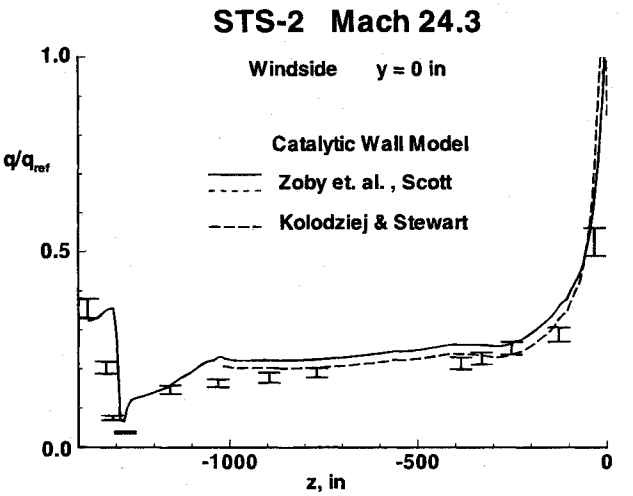

Fig. 4 Heating distribution along the windside surface centerline using two models for wall catalysis.

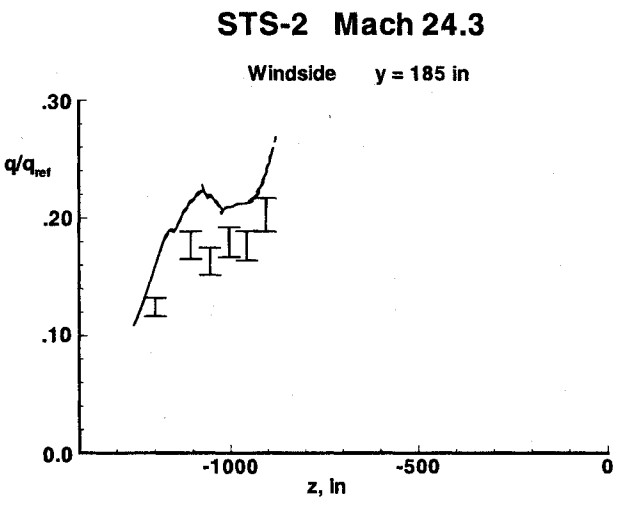

Fig. 5 Heating distribution 185 in. outboard along the windside surface.

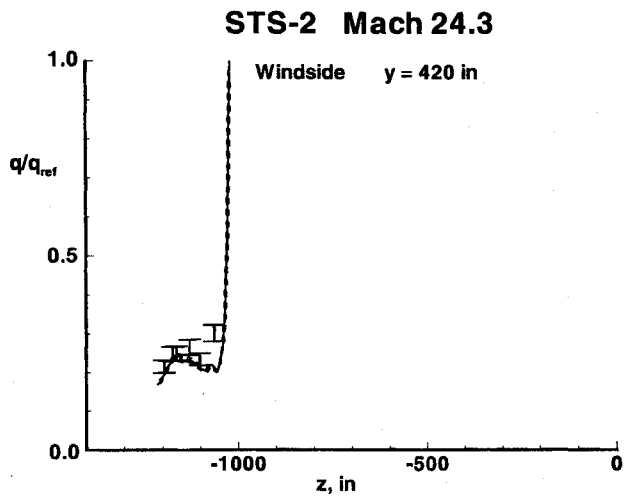

Fig. 6 Heating distribution 420 in. outboard along the windside surface.

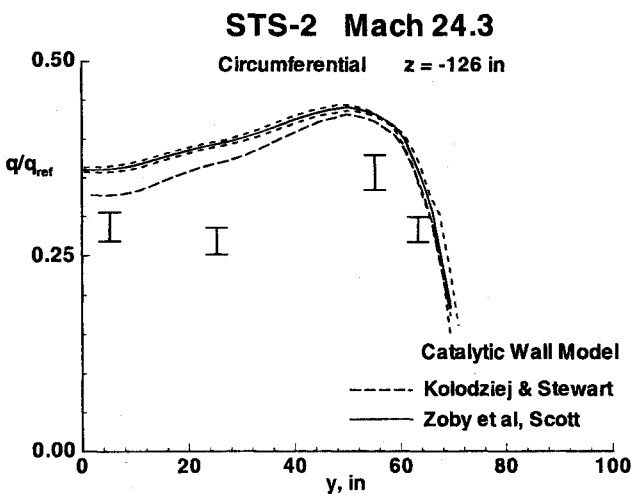

Fig. 7 Circumferential heating distribution 126 in. behind nose.

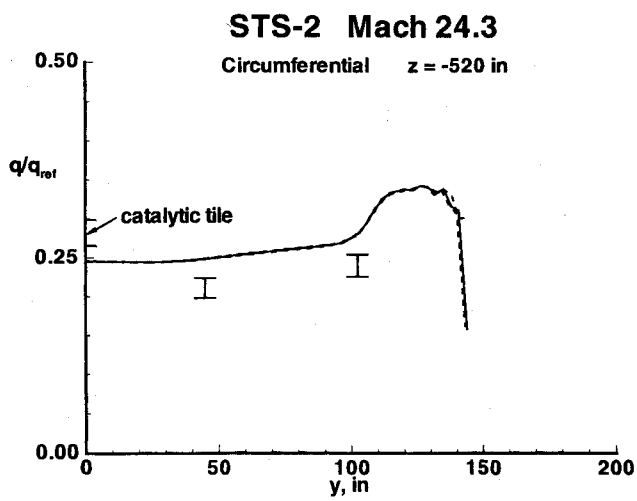

Fig. 8 Circumferential heating distribution 520 in. behind nose.

ures for each trajectory point are identically organized. First, longitudinal traces on the windside are presented starting at $y = 0$ in. (centerline) progressing outward to chordwise traces near the wing tip. Lateral and circumferential traces follow starting at a plane located 126 in. behind the nose and concluding along a line situated behind the elevon hinge line. Longitudinal traces along the leeside centerline and $y = 370$ in. outboard

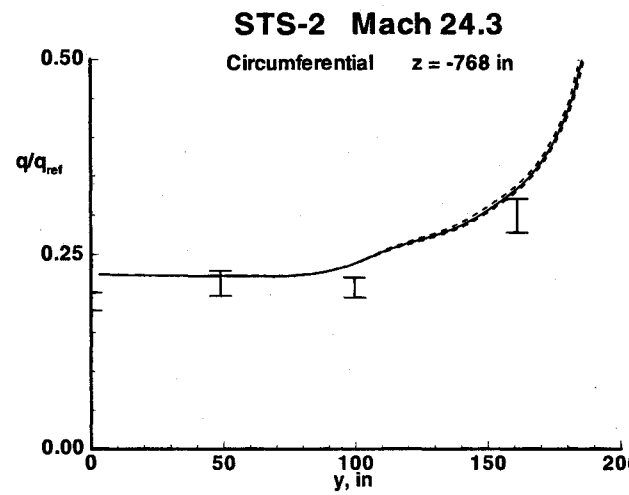

Fig. 9 Circumferential heating distribution 768 in. behind nose.

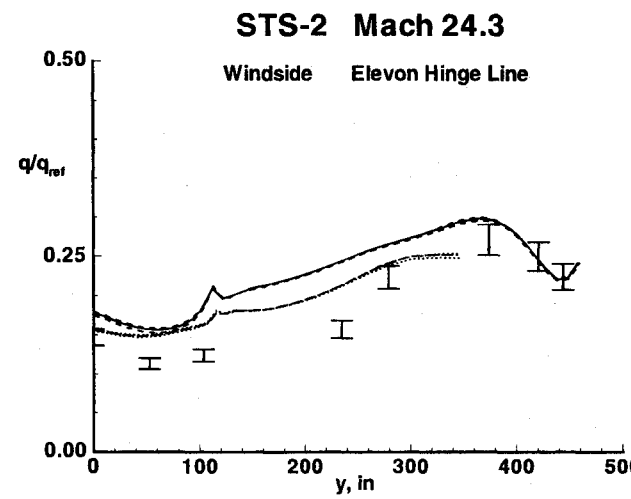

Fig. 10 Heating distribution along the windside surface from the centerline to the wingtip behind the elevon hinge line. The long dashed and dotted lines are extracted from the embedded bodyflap domain.

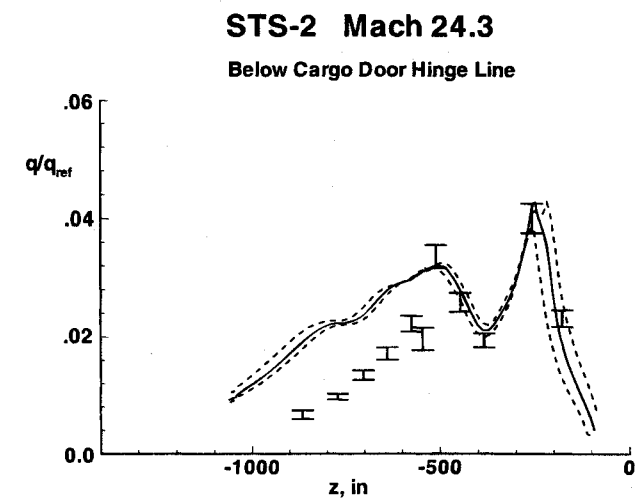

Fig. 11 Heating distribution along the fuselage below the payload door hinge line.

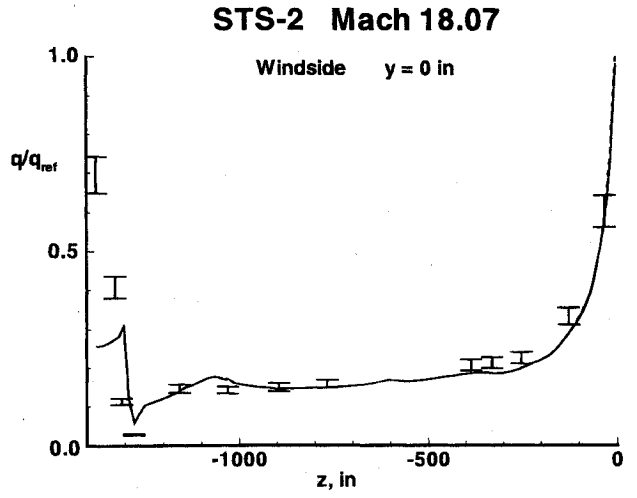

Fig. 12 Heating distribution along the windside surface centerline.

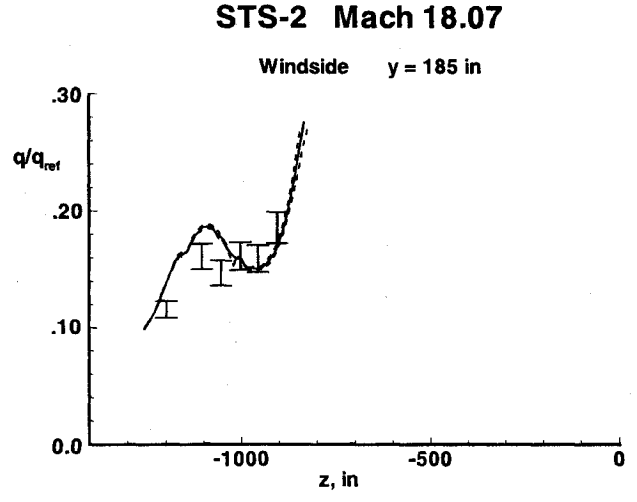

Fig. 13 Heating distribution 185 in. outboard along the windside surface.

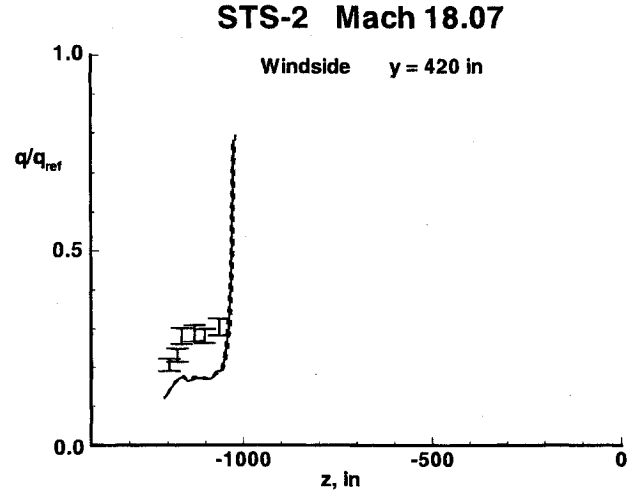

Fig. 14 Heating distribution 420 in. outboard along the windside surface.

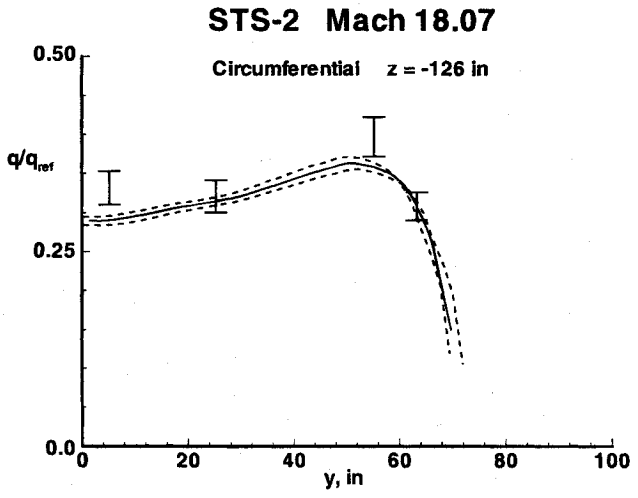

Fig. 15 Circumferential heating distribution 126 in. behind nose.

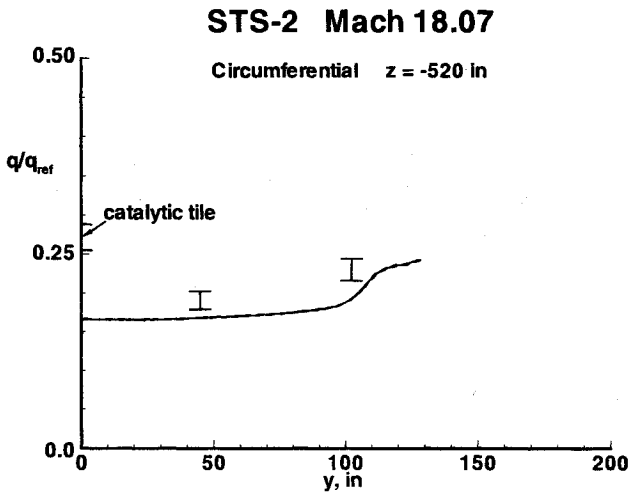

Fig. 16 Circumferential heating distribution 520 in. behind nose.

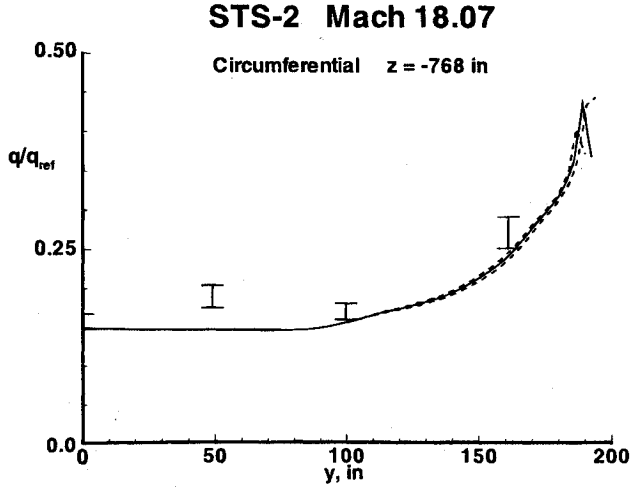

Fig. 17 Circumferential heating distribution 768 in. behind nose.

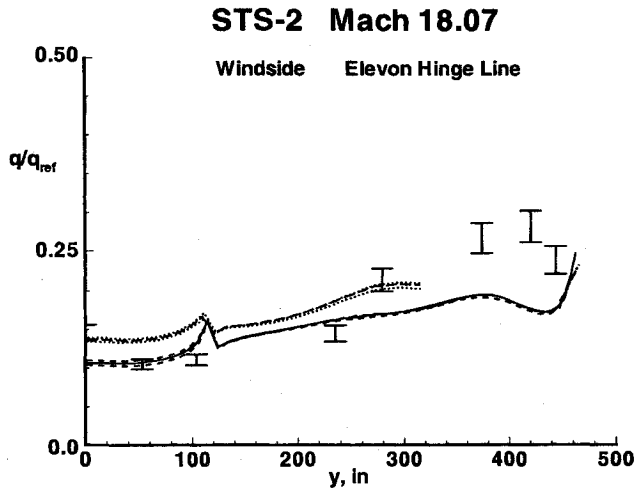

Fig. 18 Heating distribution along the windside surface from the centerline to the wingtip behind the elevon hinge line. The long dashed and dotted lines are extracted from the embedded bodyflap domain.

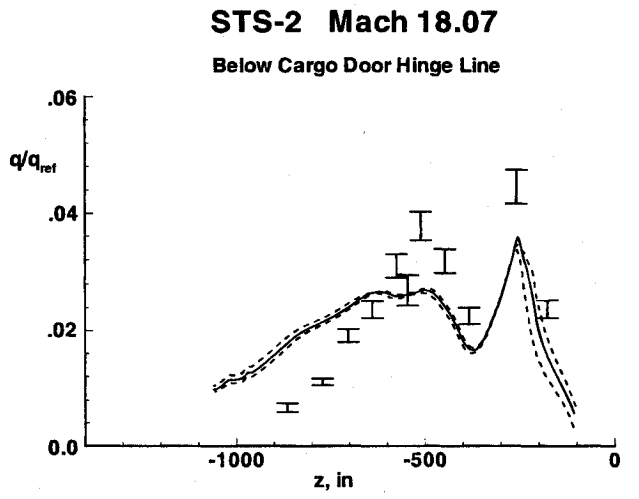

Fig. 21 Heating distribution along the fuselage below the payload door hinge line.

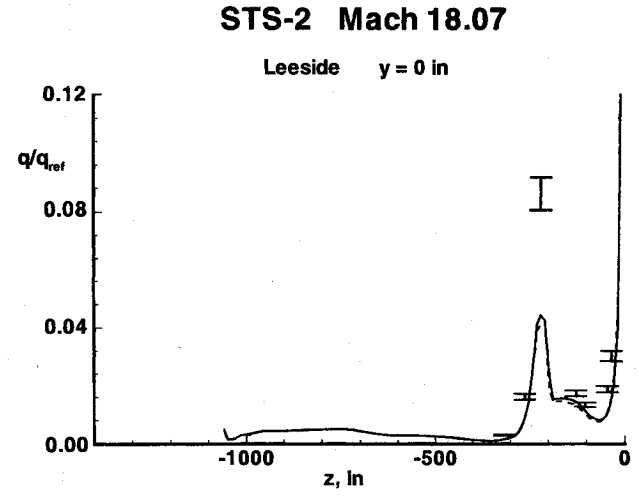

Fig. 19 Heating distribution along the leeside surface centerline.

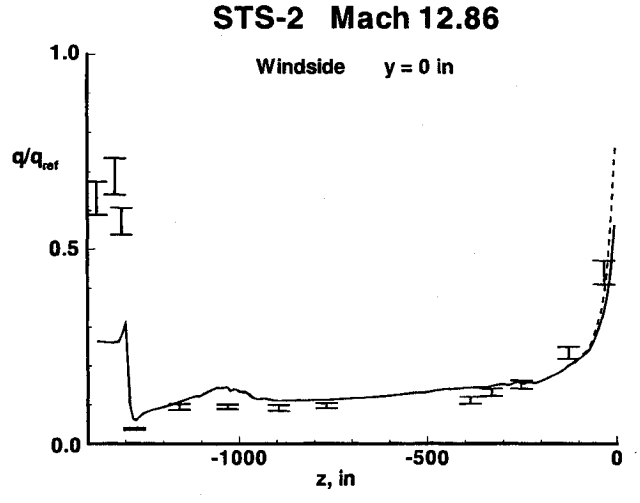

Fig. 22 Heating distribution along the windside surface centerline.

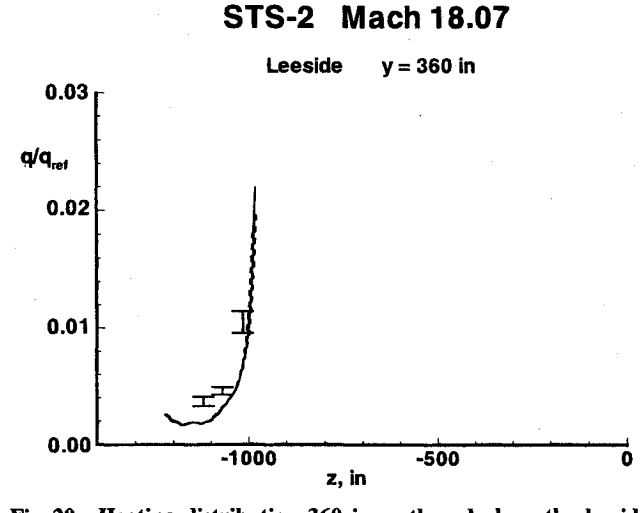

Fig. 20 Heating distribution 360 in. outboard along the leeside wing surface.

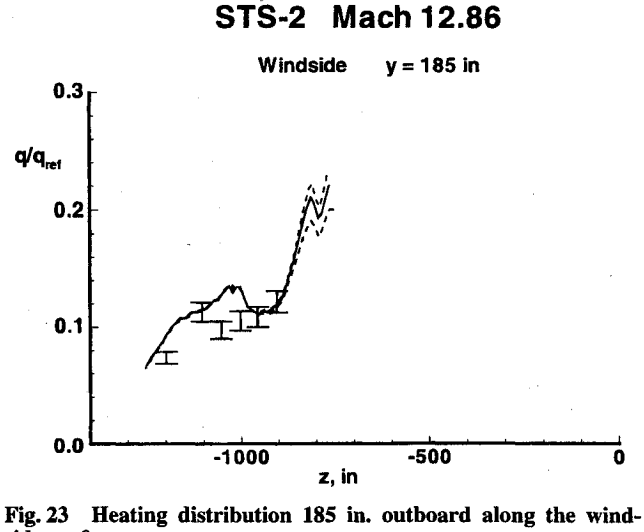

Fig. 23 Heating distribution 185 in. outboard along the windside surface.

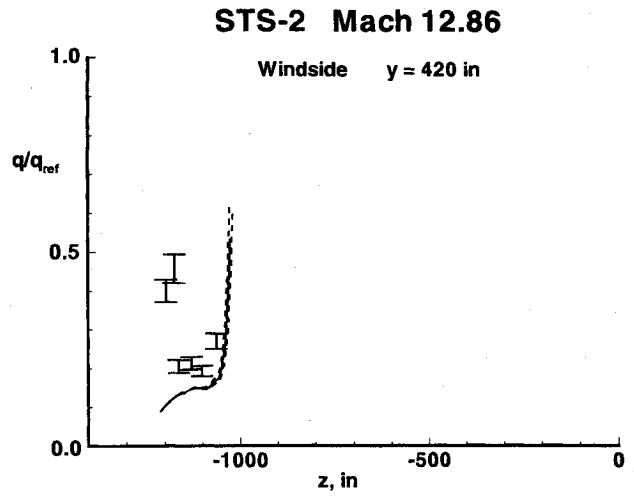

Fig. 24 Heating distribution 420 in. outboard along the windside surface.

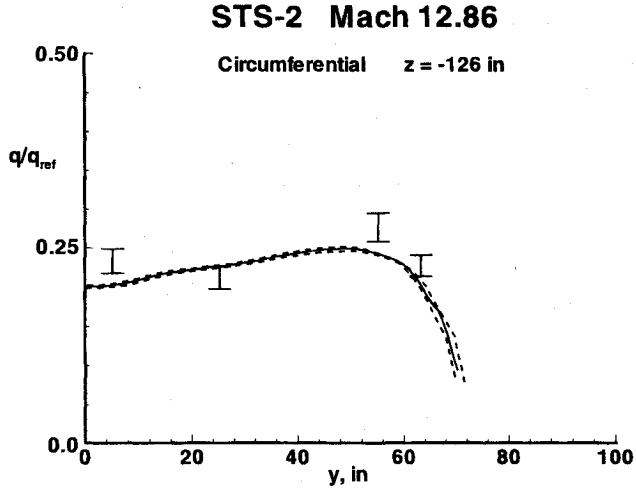

Fig. 25 Circumferential heating distribution 126 in. behind nose.

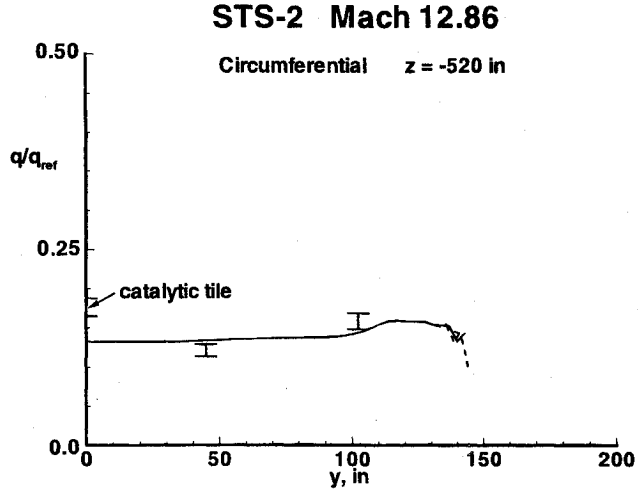

Fig. 26 Circumferential heating distribution 520 in. behind nose.

on the wing leeside then follow. (These traces are presented only for the Mach 18.07 case. The other cases show similar agreement.) Finally, longitudinal traces above and below the payload bay door hinge line are presented. Comparisons are not presented with the thermocouple data on the OMS pods and the tail because the grid was not adequate for boundary-layer resolution, as discussed in an earlier section.

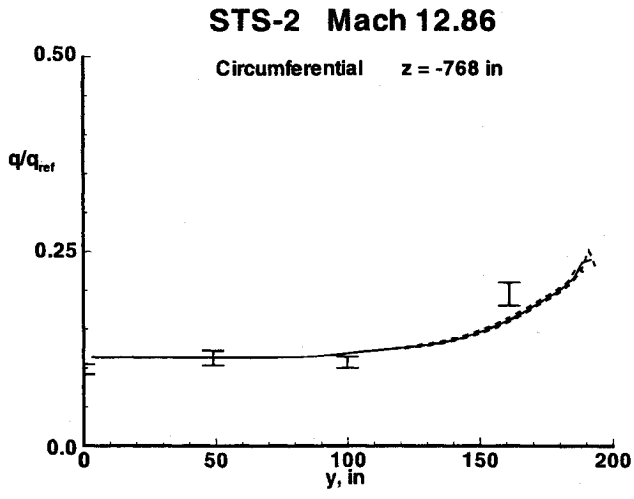

Fig. 27 Circumferential heating distribution 768 in. behind nose.

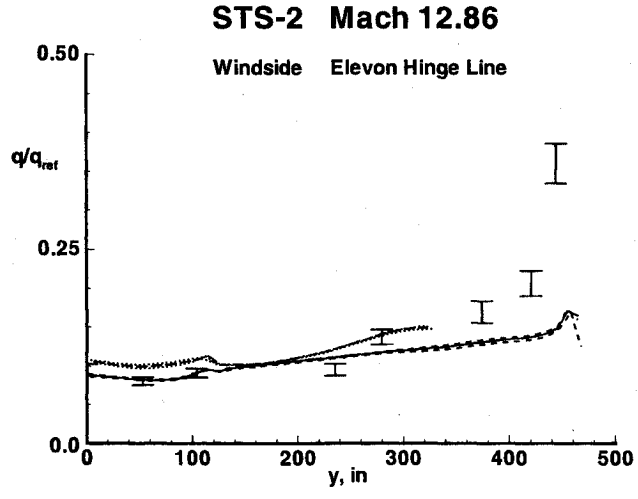

Fig. 28 Heating distribution along the windside surface from the centerline to the wingtip behind the elevon hinge line. The long dashed and dotted lines are extracted from the embedded bodyflap domain.

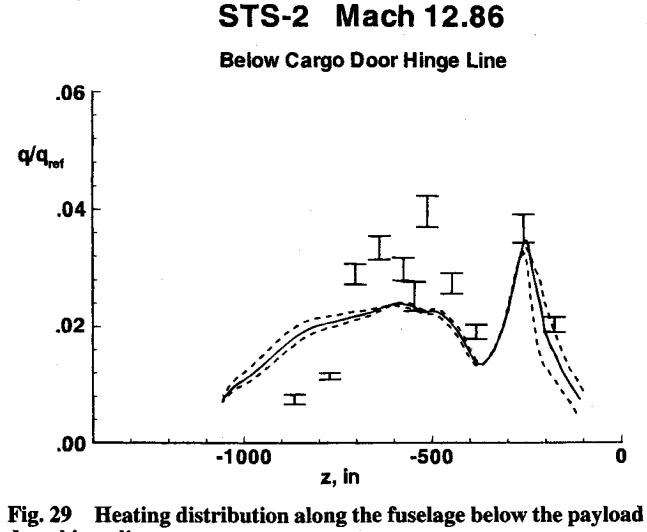

Fig. 29 Heating distribution along the fuselage below the payload door hinge line.

The solid lines denote calculated results along the center of the data trace. Because thermocouples do not generally lie along a perfect line, dashed lines denote calculated results three-to-four inches to the right or left of the center of the trace and encompass the actual location of all thermocouples along the trace. An additional set of lines is presented in the figures showing heating along the elevon hinge line. These lines denote the calculated results along the identical trace extracted from the embedded bodyflap domain. The error bar associated with the flight data, taken from Ref. 11, is a root sum square of uncertainties in the measurement. All thermocouples were calibrated before the STS-1 flight and never checked again.

Rather then stepping through each individual figure, some general observations follow. The baseline model overpredicts heating over much of the windside centerline trace at Mach 24.3 by approximately 15%. A different model for wall catalysis, discussed in a later section, improves agreement to within approximately 7%. Agreement using the baseline model along this same trace is excellent at Mach 18.07 and within 8% at Mach 12.86. The heating rise on the deflected bodyflap at Mach 24.3, beginning at $z = -1300$ in., has the correct magnitude, but precedes the rise indicated by the flight data. Such behavior could be explained by underpredicting the extent of separation; however, a grid refinement study (see later section) showed no change in the onset of the heating rise. The hinge-line area is modeled without any gaps or surface discontinuities and the possible effect of real geometry on this behavior is unknown. Transitional flow (laminar to turbulent) is evident from the time history of the thermocouple data on the bodyflap at the other trajectory points in this study.

The other streamwise traces over the windside at Mach 24.3 are in very good agreement with the flight data, with average differences less than 10%. Streamise traces out on the wing at Mach 18.07 show somewhat larger average differences. At Mach 12.86, these same comparisons improve again, except for thermocouples on the deflected elevons, which measure transitional flow as indicated by the time history of the thermocouple data.

Baseline circumferential heating predictions at $z = -126$ in. at Mach 24.3 exceed the flight data by 20 to 30%, as shown in Fig. 7. Some improvement is noted with another wall catalytic model, discussed in a later section. Calculations at subsequent points in the trajectory are in excellent agreement with flight data along this same cut.

The embedded bodyflap solution, as shown in Figs. 10, 18, and 28 show differences as large as 20% compared to the bodyflap free solution behind the elevon hinge line. The differences diminish at lower Mach numbers. The calculated solutions were expected to be closer together, showing little influence of the deflected bodyflap so far upstream, well beyond the boundary-layer separation point. The evaluation of the limiter function is somewhat altered at the inflow and side boundaries, which may have had a larger than expected influence on heating levels in the embedded domain. Also, the embedded domain partitions were converged to a smaller error norm (order 10^{-7}) than the full body solution because the bodyflap flowfield took longer to converge. Inboard data points are generally in good agreement with the calculations at Mach 18.07 and 12.86, with outboard locations measuring transitional effects at Mach 12.86.

Leeside centerline heating calculations are in good agreement with experimental data across the Mach number range (Fig. 19), except for an underprediction on the center post between the windows of the canopy. A rather coarse circumferential resolution of the canopy is a suspected cause of this underprediction. The slow rise in heating levels over the payload door is consistent with trends exhibited on later flights in which additional thermocouple data were available, and represents an improvement to some earlier related calculations reported in Ref. 7. Wing leeside predictions (Fig. 20) are in good agreement with the flight data across the Mach number range studied.

Baseline calculations are in good agreement with the flight data across the Mach number range for the first 400 in. along the data traces above and below the payload door hinge line. Good agreement persists longer for higher Mach numbers. A second, local peak is smoothed out at the lower Mach numbers and predictions then exceed the measured data for the trace below the payload door hinge line. A possible contributor to these differences is a grid alignment problem, discussed in a later section.

Finite-Catalytic-Wall Study

Surface heating using the finite-catalytic-wall model of Stewart et al.[16] is compared to results using the baseline model of Zoby et al.[14] at Mach 24.3. Figure 4 makes the comparison along the windside centerline. Figure 7 makes the comparison in a circumferential direction on a windside plane 126 in. behind the nose. The Stewart et al. model is derived from experimental data at wall temperatures greater than actually encountered on much of the windside ($T_{wall} > 1250$ K). The baseline model is derived from viscous shock-layer computations of the windside shuttle flow, and it is of questionable validity at wall temperatures greater than 1200 K. The Stewart et al. model predicts stronger catalytic effects for oxygen recombination than the baseline model at temperatures greater than $\approx$ 1300 K. The baseline model is more catalytic below these temperatures. The relative heating levels predicted by the two models is consistent with this crossover point. Differences between the two models, particularly in the stagnation region, are exacerbated because of the differences in the radiative equilibrium wall temperatures. (Higher wall temperatures further enhance catalytic efficiencies.) The present results indicate a slight improvement of the comparison to flight data using the Stewart et al. model on the centerline and circumferential plots.

Grid Convergence Study and Error Estimates

As noted earlier, the grid distribution function and number of cells in the normal direction are based on grid convergence studies in Refs. 6 and 12. These earlier studies, which focused on centerline and stagnation point heating, indicate that the present results should be within approximately 8% of a grid converged solution (based strictly on normal grid convergence studies) as discussed previously. There is no numerical evidence to suggest this estimate is valid for the flow downstream of the bow-shock–wing-shock interaction region in the present case.

Resource limitations precluded a full, global grid convergence test. An isolated test confined to the nose region (Fig. 30) for the Mach 24.3 case is well within the 8% error discussed earlier for heating over the entire forebody. In this case, the

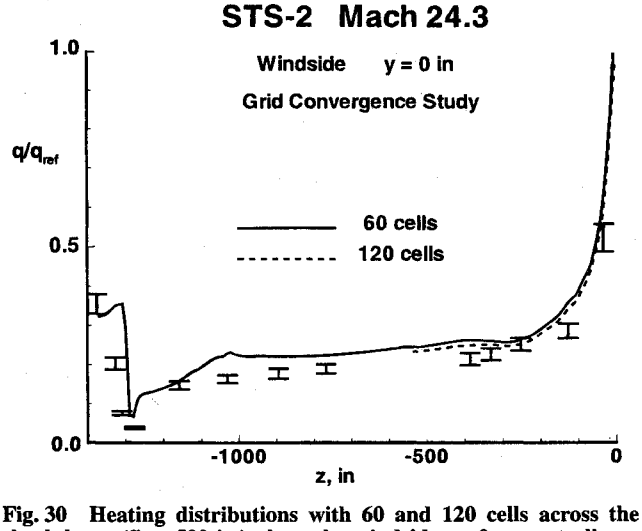

Fig. 30 Heating distributions with 60 and 120 cells across the shock layer (first 500 in.) along the windside surface centerline.

cell Reynolds number of the doubled grid case was equal to 3.0, as in the baseline case, but twice the number of points allowed improved resolution of the boundary layer and shock layer, resulting in a smaller maximum cell growth factor. (Large cell growth factors in LAURA tend to increase surface heating with all other factors equal.[12])

Although not presented in the figures, streamwise doubling of the grid on the bodyflap with appropriate clustering at the hinge line was performed on selected bodyflap solutions. Some sharpening of the overpressure and heating on the deflected flap associated with the oblique shock impingement emanating from the boundary-layer separation point upstream of the flow is observed as compared to the baseline solution. The onset of separation occurred approximately 3 in. earlier, in the Mach 18.07 test case, with distance from separation to reattachment points extending approximately 21 in. Maximum thickness of the separation bubble above the hinge line is approximately 2 in. The effect of a glove step at the hinge line is not accounted for here. Net effects on aerodynamic coefficients were trivially small.

Baseline results on the side of the fuselage (Fig. 11) indicate that some aspect of the vortex scrubbing past 500 in. may have been smeared based on comparisons with the flight data. The smearing may indicate not so much a lack of circumferential resolution as a grid that is poorly aligned with the vortical flow on the leeside. Grid adaption to local flow phenomena with a tool such as solution adaptive grid scheme (SAGE)[23] is probably warranted in this instance, but it has not yet been tested.

The present results have demonstrated that hypersonic, laminar flow simulations over the Space Shuttle, including appropriate physical models for gas chemistry and wall catalysis, can be achieved on available supercomputers in a multiuser environment. Furthermore, the results are achieved on grids with sufficient resolution to provide credible predictions based on both comparisons to existing flight data and on grid convergence tests of related, smaller problems. Even with the present uncertainties, (which can be reduced further but never eliminated), it is believed that current CFD tools provide important benchmarking capabilities. We believe that these tools provide the most accurate ground-based predictions for aerothermal loads across this flight regime. When used in conjunction with available engineering design codes, experimental facilities, and flight tests, a system of checks becomes available that must not be ignored in the design of future elements of our space transportation system.

Concluding Remarks

A multiblock, laminar heating analysis using Program LAURA for the shuttle orbiter at three trajectory points for STS-2 ranging from Mach 24.3 to Mach 12.86 on re-entry is described. This approach enables the calculation of aerothermal loads across a realistic, winged body with approximately one million grid points using approximately 150–200 CPU hours and 128 megawords storage on a Cray Y-MP. The correct elevon and bodyflap deflections are included for each trajectory point. The multiblock relaxation strategy partitions the flowfield into manageable blocks with appropriate boundary conditions requiring a fraction of the computational resources (time and memory) required by a full domain approach. Converged blocks are eventually reassembled to enable a fully coupled converged solution over the entire vehicle, starting from a nearly converged initial condition. The entire two stage process is estimated to be a factor ten times faster than a conventional, global relaxation approach for this application.

The baseline gas model for air assumes chemical nonequilibrium with seven species and thermal equilibrium. A finite-catalytic-wall model appropriate for Shuttle tiles at a radiative equilibrium wall temperature is applied. Additional tests at selected points involve thermal nonequilibrium models, chemical equilibrium models, and variations on the gas kinetic model and catalytic wall model. Gas-kinetic model variations make little difference on aerodynamics and heating, except in the vicinity of the wing leading edge. Average differences in calculated heating levels between the two wall catalysis models studied are approximately 10%, where differences in the wall temperatures associated with the radiative equilibrium wall boundary condition magnify this effect. The present results are expected to be within 8% of grid converged values in the stagnation region and windside centerline. Grid refinement confined to the forward part of the shuttle confirm this estimate. Grid-related errors may be larger downstream of the bow-shock–wing-shock interaction and associated with the leeside vortical flow, but these have not been quantified in this work.

Comprehensive comparisons to flight data along 10 linear cuts on the windside and leeside surfaces and three trajectory points are presented. Computed heating levels are generally in good agreement with the flight data and lie within the estimated experimental and numerical error bands, although a few rather large discrepancies remain unexplained.

References

[1] Lee, D. B., and Harthun, M. H., "Aerothermodynamic Entry Environment of the Space Shuttle Orbiter," AIAA Paper 82-0821, June 1982.

[2] Goodrich, W. D., Li, C. P., Houston, C. K., and Olmeda, L., "Numerical Computations of Orbiter Flowfields and Laminar Heating Rates," *Journal of Spacecraft and Rockets*, Vol. 14, No. 5, 1977, pp. 257–264.

[3] "Shuttle Performance: Lessons Learned," NASA CP 2283, 1983, pp. 719–864.

[4] Häuser, J., Muylaert, J., Wong, H., and Spel M. "Aerothermodynamic Calculations for the Space Shuttle Orbiter," AIAA Paper 92-2953, July 1992.

[5] Wada, Y., and Kubota, H., "Numerical Simulation of Re-Entry Flow around the Space Shuttle with Finite-Rate Chemistry," International Symposium on Space Technology and Science, Tokyo, May 20–25, 1990.

[6] Weilmuenster, K. J., and Gnoffo, P. A., "Solution Strategies and Heat Transfer Calculations for Three-Dimensional Configurations at Hypersonic Speeds," AIAA Paper 92-2921, July 1992.

[7] Kleb, W. L., and Weilmuenster, K. J., "Characteristics of the Shuttle Orbiter Leeside Flow During a Reentry Condition," AIAA Paper 92-2951, July 1992.

[8] Weilmuenster, K. J., Gnoffo, P. A., and Greene, F. A., "Navier-Stokes Simulations of Orbiter Aerodynamic Characteristics Including Pitch Trim and Bodyflap," AIAA Paper 93-2814, July 1993.

[9] Gnoffo, P. A., Gupta, R. N., and Shinn, J., "Conservation Equations and Physical Models for Hypersonic Air Flows in Thermal and Chemical Nonequilibrium," NASA TP 2867, Feb. 1989.

[10] Gnoffo, P. A., "Point-Implicit Relaxation Strategies for Viscous, Hypersonic Flows," *Computational Methods in Hypersonic Aerodynamics*, edited by T. K. S. Murthy, Computational Mechanics Publications, Kluwer Academic Publishers, Hingham, MA, 1991, pp. 115–151.

[11] Hartung, L. C., and Throckmorton, D. A., "Space Shuttle Entry Heating Data Book Volume I—STS-2," NASA Rept. 1191, Parts 1 and 2, May 1988.

[12] Gnoffo, P. A., Hartung, L. C., and Greendyke, R. B., "Heating Analysis for a Lunar Transfer Vehicle at Near-Equilibrium Flow Conditions," AIAA Paper 93-0270, Jan. 1993.

[13] Gnoffo, P. A., "Asynchronous, Macrotasked Relaxation Strategies for the Solution of Viscous, Hypersonic Flows," AIAA Paper 91-1579, June 1991.

[14] Zoby, E. V., Gupta, R. N., and Simmonds, A. L., "Temperature-Dependent Reaction Rate Expressions for Oxygen Recombination," *Thermal Design of Aeroassisted Orbital Transfer Vehicles*, edited by H. F. Nelson, Vol. 96, Progress in Astronautics and Aeronautics, AIAA, New York, 1985, pp. 445–464.

[15] Scott, C. D., "Catalytic Recombination of Nitrogen and Oxygen on High-Temperature Reusable Surface Insulation," *Aerothermodynamics and Planetary Entry*, edited by A. L. Crosbie, Vol. 77, Progress in Astronautics and Aeronautics, AIAA, New York, 1981, pp. 192–213.

[16] Stewart, D. A., Leiser, D. B., Kolodziej, P. and Smith, M., "Thermal Response of Integral Multicomponent Composite Thermal Protection Systems," AIAA Paper 85-1056, June 1985.

[17] Park, C., *Nonequilibrium Hypersonic Aerothermodynamics*, Wiley, New York, 1990.

[18] Dunn, M. G., and Kang, S. W., "Theoretical and Experimental Studies of Reentry Plasmas," NASA CR-2232, April 1973.

[19] Gupta, R. N., Yos, J. M., Thompson, R. A., and Lee, K. P., "A Review of Reaction Rates and Thermodynamic and Transport Properties for an 11-Species Air Model for Chemical and Thermal Nonequilibrium Calculations to 30,000 K," NASA Rept. 1232, Aug. 1990.

[20] Srinivasan, S., Tannehill, J. C., and Weilmuenster, K. J., "Simplified Curve Fits for the Thermodynamic Properties of Equilibrium Air," NASA Rept.-1181, Aug. 1987.

[21] Gupta, R. N., Lee, K. P., Thompson, R. A., and Yos, J. M., "Calculations and Curve Fits of Thermodynamic and Transport Properties for Equilibrium Air to 30,000 K," NASA Rept.-1260, Oct. 1991.

[22] Greene, F. A., and Gupta, R. N., "Viscous Equilibrium Computations Using Program LAURA," *Journal of Spacecraft and Rockets*, Vol. 29, No. 5, pp. 627–632.

[23] Davies, C., and Venkatapathy, E., "Application of a Solution Adaptive Grid Scheme, SAGE, to Complex Three-Dimensional Flows," AIAA Paper 91-1594, June 1991.